

**Biophysical Journal, Volume 114**

**Supplemental Information**

**Multimodal Measurements of Single-Molecule Dynamics Using  
FluoRBT**

**Ivan E. Ivanov, Paul Lebel, Florian C. Oberstrass, Charles H. Starr, Angelica C. Parente, Athena Ierokomos, and Zev Bryant**

# Supporting Material

## Table of Contents

<b>Methods</b> .....	2
<b>Figure S1.</b> Optical schematic of fluorescence excitation and emission paths .....	6
<b>Figure S2.</b> Demonstration of imaging with FluoRBT .....	7
<b>Figure S3.</b> Camera synchronization.....	8
<b>Figure S4.</b> Extension resolution of FluoRBT .....	9
<b>Figure S5.</b> Fluorescence and extension changes at the B-Z transition .....	10
<b>Figure S6.</b> Model for the dependence of dye separation on torque .....	12
<b>Figure S7.</b> FRET efficiency measurements of the d(pGpC) <sub>11</sub> sequence of interest immobilized on a surface..	14
<b>Figure S8.</b> High-resolution FRET measurements via alignment to mechanical data.....	15
<b>Note 1.</b> Building blocks for DNA tethers .....	17
<b>Table S1.</b> PCR primers, templates, and restriction enzymes used for tether construction .....	18
<b>Table S2.</b> DNA oligonucleotides used for tether construction .....	18
<b>Note 2.</b> List of parts .....	19
<b>References</b> .....	20

## Methods

**Instrumentation.** Experiments were performed on a custom-built evanescent darkfield microscope, as previously described (1). The instrument was modified for fluorescence microscopy by constructing an additional optical path for excitation with 532 nm and 633 nm light (Fig. S1). In the experiments described here, fluorophores were excited with only 532 nm light. Rotor bead scattering was imaged on a CMOS camera (Mikrotron EoSens CL) at 2000 Hz for hairpin opening experiments (Fig. 1 and Fig. 3), and at 250 Hz for studying the B-Z DNA transition (Fig. 2). Fluorophore emission was imaged on an EMCCD camera (Andor iXon+ 897) at 100 Hz for postsynchronization experiments, at 20 Hz for hairpin opening experiments, and at 5 Hz for studying the B-Z DNA transition. Acquisition from the two cameras was synchronized via TTL triggers (Fig. S3). Brightfield imaging of the magnetic bead was not performed simultaneously with fluorescence and scattering measurements, but was used separately for force calibration as in previous work (1), and for approximate spatial alignment of the two cameras. Focus stabilization (1) was run at 4 Hz after choosing the focal plane that minimizes coupling between the evanescent nanometry signal and the z-motion of the microscope stage (see Supplementary Figure 9 in Ref. (1)). Hairpin opening experiments were performed under  $\sim 8$  pN of tension, such that the open and closed states were approximately equally probable.

**Fluorescence illumination conditions.** We used sample irradiance of  $\sim 500$  W/cm<sup>2</sup> for typical hairpin opening experiments (Fig. 1), and  $\sim 50$  W/cm<sup>2</sup> for studying the B-Z DNA transition (Fig. 2) and for postsynchronizing fluorescence data to mechanical data (Fig. 3). We used approximately s-polarized fluorescence excitation light for all experiments (Fig. S1), and fluorophore intensities can depend on dipole orientation. Switching to circular polarization in the excitation beam only partially alleviates anisotropic effects in typical TIRF illumination geometries, although alternative designs have been developed to achieve near-isotropic excitation (2). In hairpin opening experiments shown here, dye attachment via flexible linkers (see Note 1 and Table S2) is expected to allow orientational averaging through rapid rotation of the dyes (3). In the d(pGpC)<sub>11</sub> construct, fluorescent dyes are incorporated into the DNA backbone and may experience restrained rotational mobility (refer to Fig. S6). In FRET experiments, the relative orientation of the donor dipole with respect to the

polarization axis may influence the recorded signal intensity, but the measured FRET efficiency is largely unaffected, as it depends on the ratio of the donor and acceptor intensities.

**DNA tether design.** DNA tethers were constructed by ligation of restriction enzyme digested PCR products, as previously described (1,4,5). The DNA hairpin and the d(pGpC)<sub>11</sub> sequence of interest were constructed from hybridized synthetic oligonucleotides; both sequences were adapted from model systems previously reported in the literature (6-8). The hairpin construct used in all experiments described here was 15R60/T8, with the exception of data presented in Figure S4b where 20R60/T4 was used. See Note 1 for details.

**Sample preparation.** Imaging was performed in fluidic chambers, as described before (1). Rotor beads used in these experiments were 300 nm Power-Bind streptavidin coated polystyrene particles (Thermo Fisher Scientific, 29000701011150). Hairpin opening experiments were performed in 20 mM Tris-HCl pH 8.0, 10 mM NaCl, 1 mM EDTA, 0.2% Tween-20, 0.2 mg/ml BSA, 0.01% NaN<sub>3</sub>, and 1x oxygen scavenging reagents (0.4% glucose, 1250 U/ml glucose oxidase (Sigma-Aldrich, G2133), 100 000 U/ml catalase (Sigma-Aldrich, C100), and ~2 mM Trolox (Sigma-Aldrich, 238813)). Torque-twist curves were performed in 40 mM Tris-HCl pH 8.0, 100 mM NaCl, 5 mM EDTA, 0.2% Tween-20, 0.2 mg/ml BSA, 0.01% NaN<sub>3</sub>, and 1x oxygen scavenging reagents.

**Torque spectroscopy.** Torque-twist curves (Fig. 2) were collected under 2 pN of tension. The total twist of the molecule was changed at 9°/s by rotating the magnetic tweezers. Twist was ramped from 0 rotations to -10 rotations during the unwinding phase, and then from -10 rotations to +2 rotations during the rewinding phase of the torque-twist curve. Torque was calculated based on the angular deflection of the calibrated transducer segment between the magnetic bead and the rotor bead, i.e.  $\tau = \kappa \alpha$ , where  $\kappa = 0.26 \text{ pN nm/rad}$  is the torsional stiffness of the transducer, and  $\alpha = \theta - \psi$  is the difference in angle between the magnetic bead ( $\theta$ ) and the rotor bead ( $\psi$ ). The angle of the magnetic tweezers corresponding to  $\theta = 0$  was set by maximizing the extension of the DNA tether under low force (4,5). Fluorescence excitation was turned on only for part of the rewinding cycle, due to the limited observation lifetime of the fluorophores.

**Data analysis.** Rotor bead tracking was performed as previously described (1). Briefly, the angle of the rotor bead was calculated from its x-y trajectory, and  $\Delta z$  was determined from the intensity of the rotor bead in the

evanescent field using  $\Delta z = -\Lambda \log(I/I_0)$ , where  $I_0$  is the intensity at a reference  $z$  height, and  $\Lambda$  is the evanescent field delay length (9). As described in detail previously (1),  $\Lambda$  was determined by collecting  $z$  fluctuations and cross-calibrating with dual-focus imaging (1,10), after calibrating the dual-focus method by stepping the piezo stage. For the experiments reported here, we used  $\Lambda = 210$  nm, based on averaging calibrations obtained for individual molecules.

Extension and torque data were block-averaged in bins matching the acquisition rate of the fluorescence signal. Extension data from hairpin unfolding experiments were assigned to the open or closed states by fitting the time traces to a two-state hidden Markov model (HMM) using the segmental k-means method in QuB (11). The extension at the peak of the Gaussian function fit to the closed state in each trace was set to  $\Delta z = 0$ .

Recorded intensity in the donor and acceptor channels was corrected for fluorescence background and for weak constant signal that sometimes arose from infrared excitation of the magnetic bead. Acceptor intensity was further corrected for spectral cross-talk from the donor channel and for direct excitation from the donor excitation source. The  $\gamma$  factor, accounting for differences in quantum yield and detection efficiency between the two fluorophores, was calculated from changes in donor and acceptor intensity during hairpin opening or at the acceptor photobleaching event. FRET efficiency was calculated from  $E_{FRET} = \left(1 + \gamma I_D/I_A\right)^{-1}$ , where  $I_D$  and  $I_A$  are, respectively, the corrected donor and acceptor intensities (12). Correction factors were calculated for each individual molecule when possible; otherwise average values from ensemble measurements were used. We defined  $I_A = 0$  in the open hairpin state due to the large spatial separation between the two dyes.

**Data selection.** We followed DNA tether selection criteria as described in Lebel et al. (1), except that rotor beads showing unconstrained angular fluctuations were selected for DNA hairpin tethers, consistent with the design. We verified that the hairpin construct showed reversible transitions in  $\Delta z$  before collecting FluoRBT measurements. For hairpin opening experiments, we collected data on 35 DNA tethers. Of those, 8 were missing a donor or an acceptor dye, 10 produced fluorescence traces shorter than 10 seconds, 2 showed low SNR, and 2 showed anomalous very slow or absent FRET transitions. In Figure 1 we report on the remaining 13 molecules. For studying the B-Z DNA transition, we collected data on 25 DNA tethers. Of those, 6 were missing a donor or an acceptor dye, 7 did not show two-state torque-twist curves, 2 showed rare intermediates

in  $E_{\text{FRET}}$  (see Fig. S7), and 2 showed short or blinking fluorescence traces. We report on the remaining 8 molecules in Figures 2, S5, and S6.

**Structural modeling.** The predicted hairpin opening distance for 15R60/T8 was calculated as the difference in extension of the 38 bases of single-stranded DNA of the hairpin in the open state (16.0 nm at 8 pN, based on the Wormlike Chain Model, using parameters  $d = 0.665$  nm/base and  $l_p = 1.14$  nm, as given in (13)) and the 2 nm width of double-stranded DNA helix of the hairpin in the closed state, giving a predicted  $\Delta z = 14.0$  nm.

The expected FRET efficiency in the closed hairpin state was determined by modeling the position of the donor and the acceptor. The dyes are attached to thymidine bases via flexible linkers, allowing for rotational mobility, and the DNA segments above and below the hairpin can swivel relative to each other (see Note 1 and Table S2). The mean dye position on 3-HNDL and 5-HNDL was derived from accessible volume (AV) calculations (3) using duplex models generated in Web 3DNA (14), linker lengths of 20 Å for the donor and 22 Å for the acceptor, linker width of 4.5 Å, and dye radius of 3.5 Å. In the calculated mean positions, the donor and the acceptor are radially displaced from the central axis of DNA by 12.0 Å and 11.5 Å, respectively. The axial separation between the dyes was calculated as 48 Å, after including 28 Å of separation between the duplex models to account for the intervening closed DNA hairpin and flanking abasic sites (see Note 1 and Table S2). Using  $R_0 = 53$  Å (15), isotropic averaging (16) over swiveling motions then yields  $E_{\text{FRET}} = 0.42$  for the closed state of the hairpin. In the open state of the hairpin, the fluorophores are much more than two Förster radii apart (~20 nm separation). We have defined  $E_{\text{FRET}} = 0$  in the open hairpin state (see above), and thus cannot determine the hairpin opening distance from FRET data.

To model the approximate donor and acceptor dye positions on the d(pGpC)<sub>11</sub> DNA helix for the geometric calculations shown in Figure S6, we generated B-DNA and Z-DNA helices using Web 3DNA (14) and then simulated average dye positions in Crystallography and NMR System (CNS) by adapting a torsion angle molecular dynamics approach described earlier (17), holding the DNA fixed while allowing dyes and linkers to fluctuate. 500 simulated annealing trials were run for each DNA model, and average dye positions were calculated based on the position of the central dye carbon in the polymethine bridge.

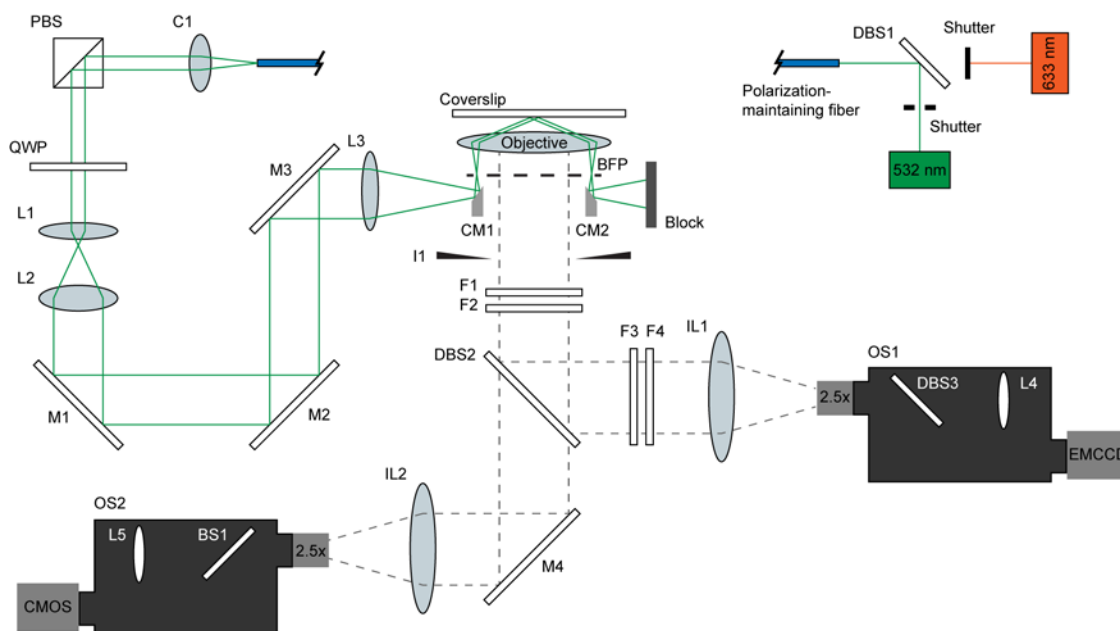


**Figure S1. Optical schematic of fluorescence excitation and emission paths.** Light from 532 nm and 633 nm lasers was coupled into a polarization-maintaining fiber. The beam at the fiber exit was collimated (C1), expanded (using lenses L1 and L2, achieving  $\sim 1500 \mu\text{m}^2$  spot at the sample), and then focused onto the objective back focal plane (BFP) via an achromatic lens (L3) and a small metallic coupling mirror (CM1). A polarizing beam splitter (PBS) and quarter-wave plate (QWP) allow adjusting the polarization of the excitation beam. This work used approximately s-polarized excitation light, as described in Methods. Two notch filters and an iris (F1, F2, and I1) were placed in the emission path to reject stray light. Fluorophore emission was spectrally separated from the longer-wavelength rotor bead scattering using a dichroic beamsplitter (DBS2). Light emitted from the dyes used in these experiments was further isolated using a 550 nm long-pass filter (F3) and 842 nm short-pass filter (F4) and then imaged through an optical splitter (OS1) onto an EMCCD camera. Emission from the donor and acceptor dyes was separated using a dichroic beamsplitter (DBS3) inserted in OS1; a weak lens (L4) was used to reduce the small focal shift between the two channels. Rotor bead scattering was also imaged through an optical splitter (OS2) onto a CMOS camera. A 50/50 beamsplitter (BS1) and a lens (L5) were inserted in OS2 during calibration of the infrared evanescent wave decay length (see Methods and Supplementary Figure 3 in Ref. (1)). Brightfield illumination of the magnetic bead (not shown) was accomplished as described earlier (see Supplementary Figure 1 in Ref (1)). For a complete list of parts, see Note 2.

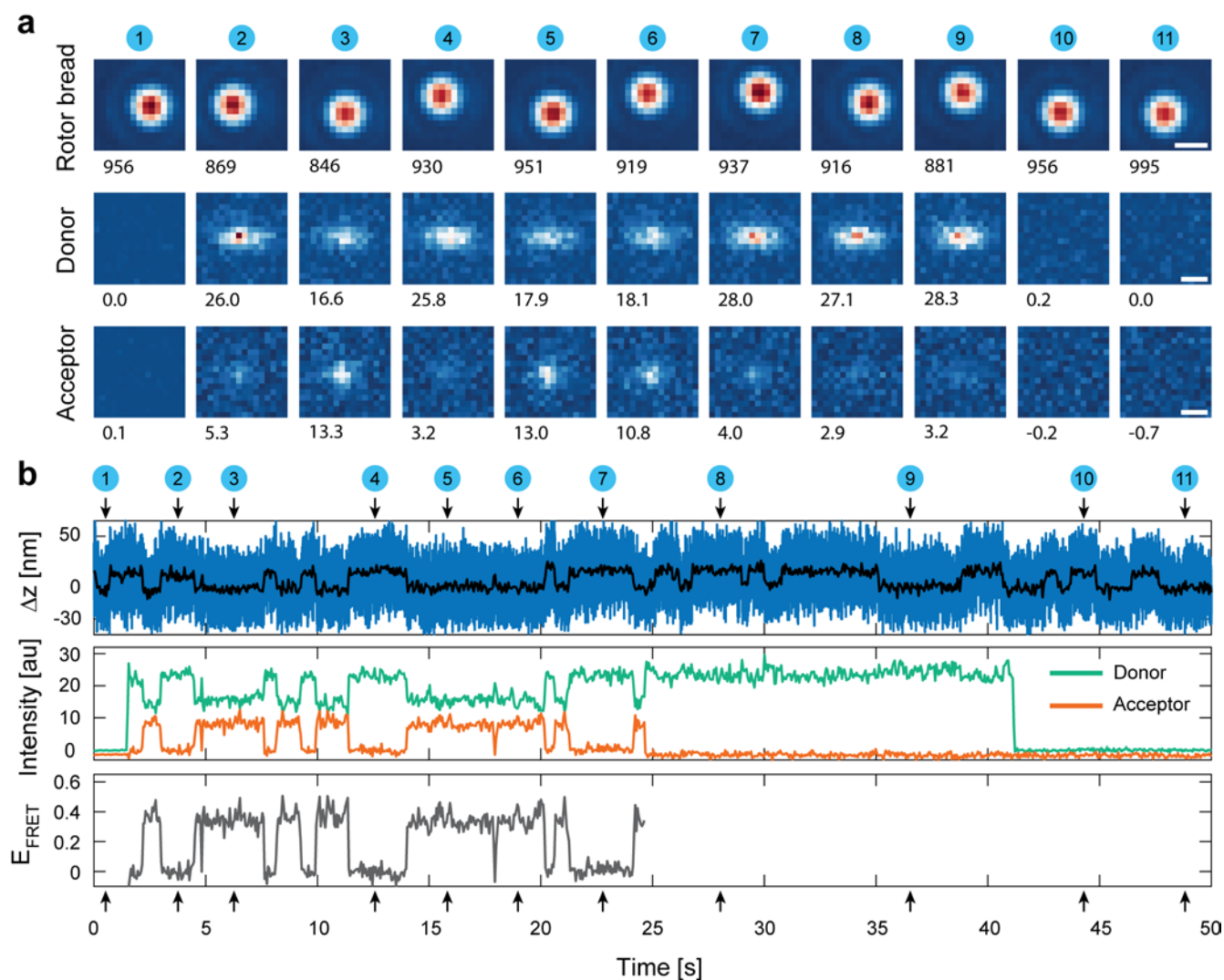


**Figure S2. Demonstration of imaging with FluoRBT.** (a) Sequence of images of the rotor bead (top) and the donor (middle) and acceptor (bottom) dyes during a FluoRBT experiment. Scale bar: 500 nm. Numbers below the images indicate the measured intensity. The donor and acceptor channels are corrected only for background signal. The donor and acceptor channels are on the same color scale, which is different from the color scale used for images of the rotor bead. Donor bleed into the acceptor channel can be seen in the images, and is corrected before plotting intensities and calculating FRET efficiencies (refer to Methods). We do not detect any signal in the donor and acceptor channels resulting from infrared excitation of the rotor bead and there is correspondingly no crosstalk between  $\Delta z$  and fluorescence intensity channels (see images and traces after both fluorophores have bleached). (b) Measurements of  $\Delta z$  (top), corrected donor and acceptor intensity (middle), and calculated FRET efficiency (bottom) for the full data set. Numbered arrows show the time point for each set of images in (a). See also Movie S1.

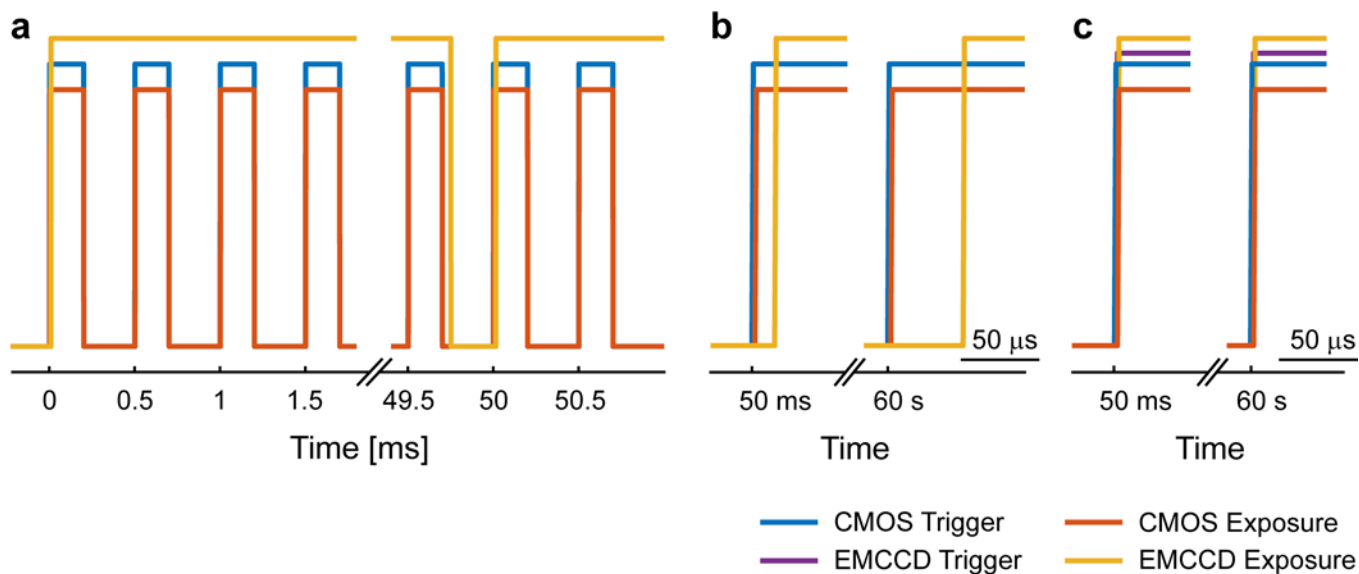


**Figure S3. Camera synchronization.** Data acquisition from the CMOS camera used for rotor bead tracking and the EMCCD camera used for fluorescence imaging was synchronized via TTL triggers generated by a National Instruments PCIe-6323 card. To validate the camera synchronization, trigger pulses and camera fire outputs (indicating camera exposure) were measured using the PCIe-6323 card at 1 MHz. (a) For experiments reported in this manuscript, exposure of the CMOS camera was initiated at the rising edge of the trigger pulse train and terminated at the falling edge. The EMCCD camera was programmed to start acquisition at the first rising edge of the CMOS trigger pulse train and then continued imaging at a pre-set framerate and exposure time. The CMOS fire output goes to the high state within 1  $\mu\text{s}$  of the trigger signal. The EMCCD fire output goes to the high state 14  $\mu\text{s}$  after the trigger signal. This delay is negligible, even at the highest bandwidth used for comparing fluorescence data to  $\Delta z$  measurements – 100 Hz (Fig. S4b). For this demonstration, microscope cameras were programmed as for hairpin opening experiments, i.e. 2000 Hz imaging of the rotor bead using the CMOS camera and 20 Hz imaging of the fluorophores using the EMCCD camera. (b) Acquisition by the EMCCD camera drifts at  $\sim 0.7 \mu\text{s/s}$  relative to the CMOS camera due to drift between the PCIe-6323 clock and the internal EMCCD camera clock. This leads to delays in exposure up to  $\sim 640 \mu\text{s}$  for the longest traces presented in this manuscript (Figure 2, 890 s); this delay is negligible for these data, as fluorescence is recorded at 5 Hz, and the angular measurements are limited by the rotor bead's rotational relaxation time of  $\sim 200 \text{ ms}$ . In the traces presented in Figure 3 and Figure S8, there will be  $\sim 330 \mu\text{s}$  delay in exposure between the two cameras by the end of the acquisition, equivalent to  $\sim 3\%$  of the 10 ms integration time used for fluorescence exposures and block-averaged extension data. (c) Acquisition by the two cameras can be synchronized to  $< 1 \mu\text{s}$  using two trigger pulse trains generated by the PCIe-6323 card based on the same master clock. This improved synchronization method was not used for collecting data for this manuscript, but is currently implemented on our instrument and is appropriate for more demanding experiments.

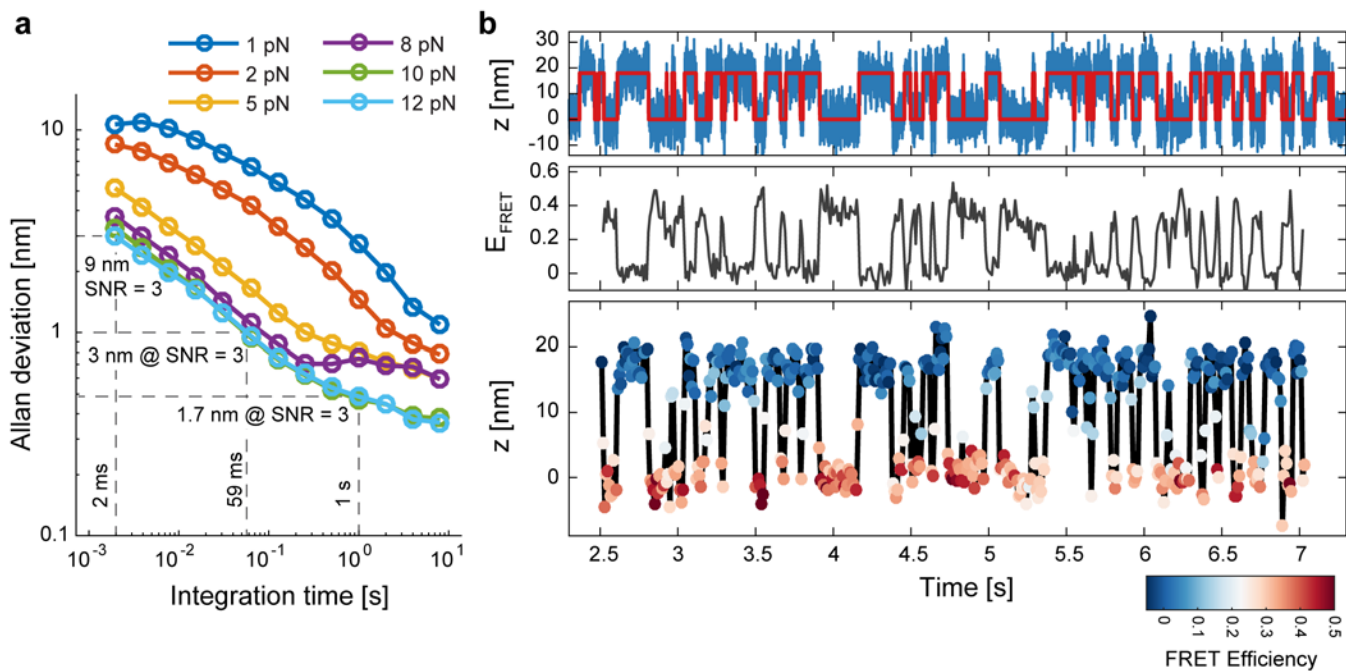


**Figure S4. Extension resolution of FluorBT.** (a) The Allan deviation in  $\Delta z$  was computed as a function of integration time for a DNA tether with a 300 nm rotor bead  $\sim 800$  bp away from the surface. The Allan deviation decreases with force due to suppression of axial fluctuations of the bead. Horizontal lines indicate the resolution in  $\Delta z$  that can be achieved in the given integration time at high force. Extension noise varies between molecules, and can be lower or higher than seen in panel (a) for individual tethers. For example, the data in Figure 1d show 3-4x higher noise at 50 ms integration time and  $\sim 8$  pN of tension, and panel (b) here shows a tether with somewhat lower noise. (b) FluorBT measurements on a 20R25/T4 hairpin tether, highlighting the spatiotemporal resolution achievable with the instrument (Allan deviation of 2.2 nm in 1 ms integration time). Compared with 15R60/T8 (Fig. 1 and Fig. 3), the 20R25/T4 hairpin shows faster transitions between the open and closed states ( $\tau_{open} = 67$  ms and  $\tau_{closed} = 53$  ms, in agreement with Woodside et al. ( $\tau_{1/2} \sim 70$  ms) (6)). Data were collected at 12 pN in buffer containing 50 mM MOPS pH 7.5, 200 mM KCl, 0.2% Tween-20, 0.2 mg/ml BSA, and 1x oxygen scavenging reagents. Top: Extension data (5000 Hz, blue) allow confident identification of the hairpin state (HMM fit – red). Middle: FRET efficiency of the dye pair (100 Hz) was calculated from the collected donor and acceptor intensities. Bottom: Overlay of FRET efficiency (color scale) and block-averaged  $\Delta z$  (100 Hz, black line) shows the correspondence between the two signals.

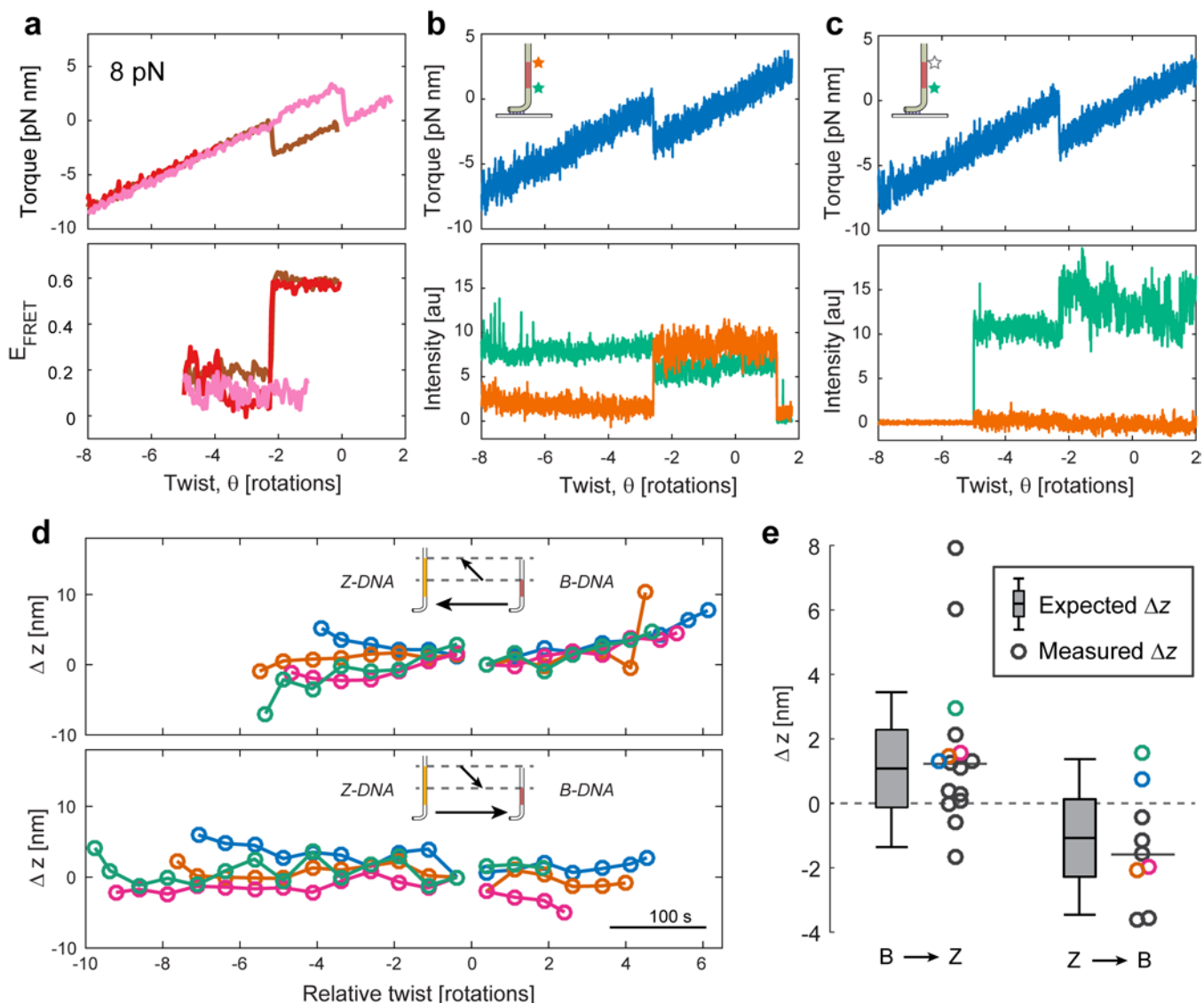


**Figure S5. Fluorescence and extension changes at the B-Z transition.** (a) FluorRBT measurements on the B-Z structural transition at increased tension (8 pN). Linear fits to the  $E_{\text{FRET}}$  versus torque data collected under 8 pN and 2 pN (Fig. 2) of tension did not show a significant difference for either B-DNA or Z-DNA state (t-test,  $p > 0.3$ ), although sampling is limited. (b) Donor and acceptor intensities show anticorrelated changes as a function of twist in the molecule, consistent with structural rearrangements in the SOI. At the B-Z transition, we observe a smaller change in donor intensity compared to the change in intensity of the acceptor. Data from this trace are also plotted in blue in Figure 2. (c) In the absence of an acceptor, we observe an increase in donor intensity as the SOI transitions from Z-DNA into B-DNA, in the opposite direction from the intensity change in the presence of a FRET acceptor, and consistent with an environment-dependent change in quantum efficiency of the dye. (d-e) Measuring the change in extension associated with the B-Z transition in the SOI. (d) Changes in extension of the rotor bead as a function of twist during the unwinding (top, SOI transitions from B- to Z-DNA) and rewinding (bottom, SOI transitions from Z- to B-DNA) regions of the torque-twist curve. Low-frequency noise obscures nanometer-scale features over the long timescales of the experiments, but the jump

in extension upon B-Z conversion can be investigated by aligning traces at the B-Z transition. Extension data were block-averaged in 30 s (0.75 rotation) bins starting at the B-Z transition, as detected from the torque channel, and zeroed at the first point before the transition. Data shown are for molecules presented in Figure 2c-d, with matching color. (e) Extension change of the rotor bead as the SOI transitions from B- to Z-DNA (left) and vice versa (right). The 22 base pair SOI is expected to lengthen by ~1 nm as it transitions from B- to Z-DNA (gray box plot, showing expected  $\Delta z$  (band inside of box)  $\pm 1$  (top and bottom of box) and  $\pm 2$  (whiskers) Allan deviations (1.2 nm) of the data). Colored data points correspond to the first measured  $\Delta z$  after the transition in panel (d). Gray data points are from measurements on other molecules.



comparison to B-DNA (1,4,5), and is also modeled under larger absolute torques in the panel shown, reflecting the torque ranges sampled in the experiment. (c) Overlay of  $E_{\text{FRET}}$  versus torque data for measurements collected at 2 pN of tension (circles, also presented in Figure 2c-d with matching color) and at 8 pN of tension (diamonds, also presented in Figure S5a with matching color). Black lines are linear fits to combined data in B-DNA ( $E_{\text{FRET}} = -0.0042 * \tau [pN nm] + 0.59$ ) and in Z-DNA ( $E_{\text{FRET}} = -0.015 * \tau [pN nm] + 0.16$ ). The obtained zero-torque  $E_{\text{FRET}}$  values are consistent with ensemble measurements of surface-immobilized partial constructs containing the portion of DNA tether below the SOI (Fig. S7,  $E_{\text{FRET}} = 0.63 \pm 0.07$  in B-DNA and  $E_{\text{FRET}} = 0.20 \pm 0.11$  in Z-DNA), and with measurements on a similar construct by Lee et al. ( $E_{\text{FRET}} = 0.50 \pm 0.08$  in B-DNA and  $E_{\text{FRET}} = 0.12 \pm 0.08$  in Z-DNA) (8). In Z-DNA  $E_{\text{FRET}}$  shows larger changes with torque, consistent with the increased torsional compliance of that state. Lee et al. (8) did not report on a change in FRET efficiency with superhelical density (refer to Fig. 4A), possibly due to higher noise in  $E_{\text{FRET}}$  in their measurement, which also lacked a direct torque measurement. Light blue lines are fits to a simplified model in which  $E_{\text{FRET}}$  in B- and Z-DNA states changes with torque only as a result of changes in dye separation. For this calculation,  $R_0$  is approximated as fixed (independent of torque) for each state, but is allowed to differ between B-DNA and Z-DNA.  $R_0$  is calculated from the zero-torque  $E_{\text{FRET}}$  value in (c) using the zero-torque dye separation presented in (b), giving  $R_0 = 48 \text{ \AA}$  in B-DNA and  $R_0 = 40 \text{ \AA}$  in Z-DNA. The dependence of  $E_{\text{FRET}}$  on torque is then calculated, using the constant- $R_0$  approximation in order to gauge expected FRET changes due to probe separation alone. The light blue region around the lines is calculated by adding  $\pm 2.5 \text{ \AA}$  uncertainty in the radial dye displacement from the helix. The model results suggest that in Z-DNA, the  $E_{\text{FRET}}$  dependence on torque can be partly explained by changes in dye separation alone. Changes in dipole orientation between the dyes could contribute significantly to changes in  $E_{\text{FRET}}$  as well. In B-DNA, the dye separation is not expected to change substantially with torque due to the higher torsional rigidity of that state, and the small but measurable FRET changes we observe under torque may depend on orientation effects, or increased compliance introduced by the dyes, or both. Orientation effects, including varying degrees of orientational freedom, could also contribute to the difference in apparent  $R_0$  between the B-DNA and Z-DNA states.

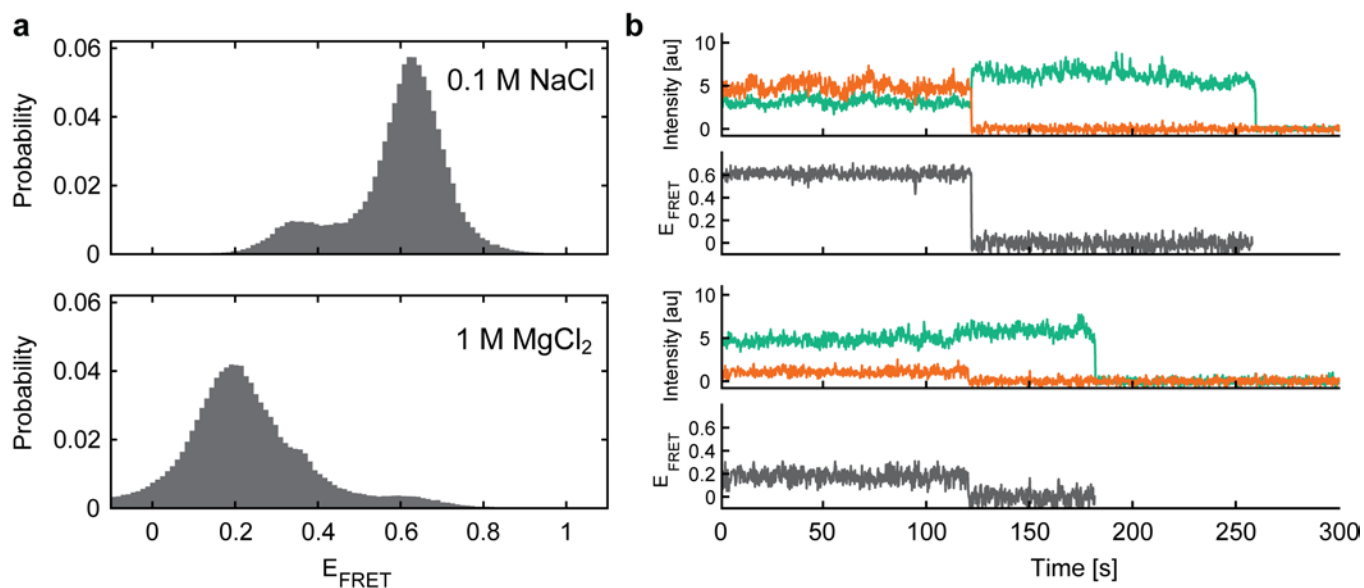


**Figure S7. FRET efficiency measurements of the  $d(pGpC)_{11}$  sequence of interest immobilized on a surface.** Partial constructs containing the GC-repeat were made by annealing and ligating the oligonucleotides MDIG, MDIG-C, F3, F4, GC-1, and GC-2 (see Note 1 and Note 2). Molecules were immobilized on an anti-digoxigenin coated surface and imaged in buffer (40 mM Tris-HCl pH 8.0, 5 mM EDTA, 0.2% Tween-20, 0.01%  $\text{NaN}_3$ , and 1x oxygen scavenging reagents) containing 0.1 M NaCl (top row) or 1M  $\text{MgCl}_2$  (bottom row) to favor, respectively, the B-DNA or the Z-DNA state of the SOI. (a) Histograms of instantaneous FRET efficiency measured under conditions favoring the B-DNA ( $n = 180$  molecules, 3.7 min average observation time) or Z-DNA ( $n = 132$  molecules, 3.6 min average observation time) state of the SOI. Only molecules containing a donor and an acceptor dye have been selected for this analysis. Gaussian mixture models were fit to the data to determine the FRET efficiencies of contributing states. Based on the major peak in each condition, the mean FRET efficiency in B-DNA is  $0.63 \pm 0.07$  and in Z-DNA is  $0.20 \pm 0.11$  (mean  $\pm$  s.d.). The additional peak at  $E_{\text{FRET}} \sim 0.36$  is attributed to an intermediate or misfolded state. (b) Example fluorescence intensity and  $E_{\text{FRET}}$  traces from molecules in B-DNA and Z-DNA state of the SOI. Data are recorded at 5 Hz.

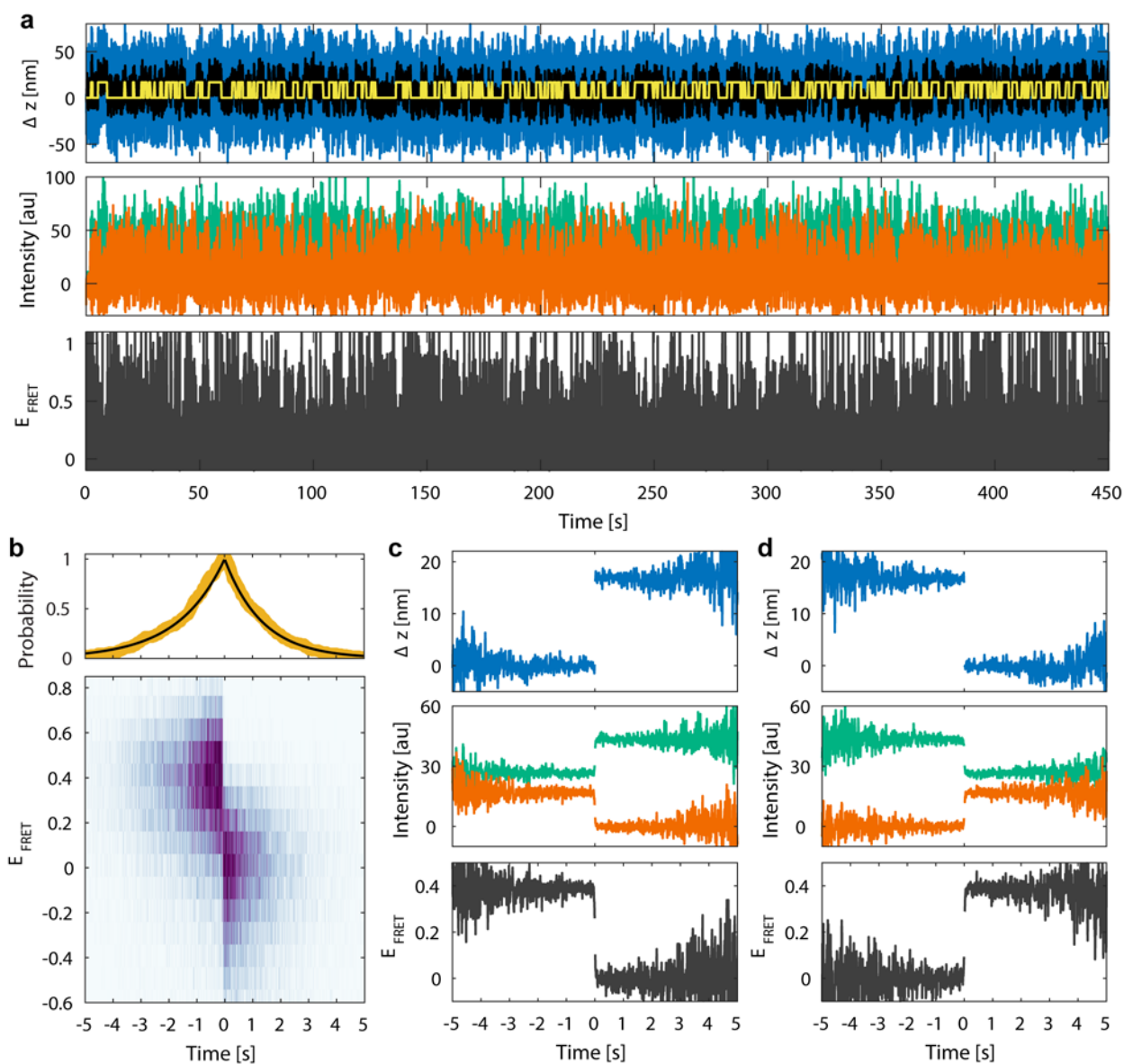
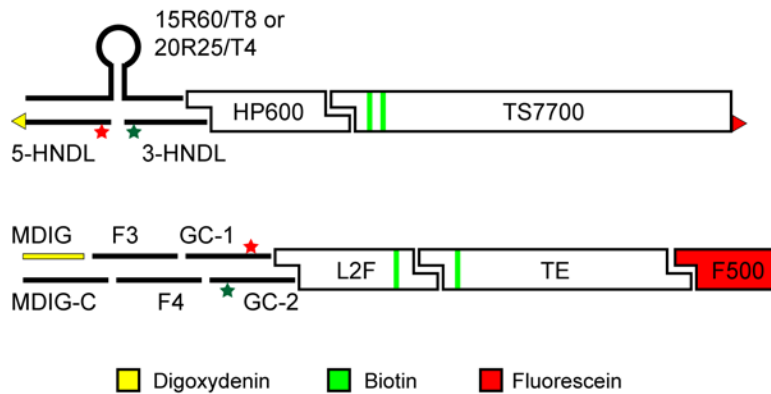


**Figure S8. High-resolution FRET measurements via alignment to mechanical data.** (a) FluorRBT trace showing many transitions between the open and closed states of a DNA hairpin. This panel is available online as a MATLAB figure file, and excerpts from this trace are also shown in Figure 3a. Top: High-resolution mechanical measurements of  $\Delta z$  (raw data – blue, and block-averaged – black) allow identification of the hairpin state (HMM fit – yellow) with SNR = 3 in  $\sim 10$  ms. Middle: Low donor excitation was used to extend the lifetime of the fluorophores, leading to poor SNR in intensity traces (donor – green, and acceptor – orange). Bottom: The calculated instantaneous FRET efficiency shows high measurement noise. (b-d) Data from (a) are excised into pieces containing a single transition of the hairpin (from closed to open state or vice versa) and aligned in time at the transition event. (b) Distribution of hairpin states as a function of time away from the opening event. Top: The probability of state observation (yellow points, based on HMM fit in (a)) decreases exponentially with time (black curves,  $\tau_{\text{open}} = 1.35$  s and  $\tau_{\text{closed}} = 1.68$  s) on timescales close to a previous

study using this hairpin ( $\tau_{1/2} = 1.3 \text{ s}$ ) (7). Bottom: Post-synchronized histogram of instantaneous FRET measurements. (c-d) Averaging of time-aligned traces reduces uncorrelated noise and provides high-resolution FRET measurements for each state. Data were aligned to (c) opening or (d) closing events. Fluorescence intensity changes can be detected with SNR  $\sim 1$  in the raw data (a) and with SNR  $\sim 13$  in the post-synchronized data (c-d).

## Note 1. Building blocks for DNA tethers.



The schematic above depicts the building blocks used for DNA tether construction. PCR templates, primers, and restriction enzymes used for construction of linear DNA pieces are given in Table S1. Synthetic oligonucleotides used in making of the DNA hairpins and the  $d(pGpC)_{11}$  sequence of interest are given in Table S2. DNA modifications used for attaching the tether to the surface, the magnetic bead, or the rotor bead are color-coded (yellow – digoxigenin, green — biotin, red — fluorescein); terminal modifications are indicated by angle brackets (< for 5' and > for 3' modification). Also, /5Phos/: 5' phosphorylation, /idSp/: 1',2'-Dideoxyribose spacer, /Q570-dT/: Quasar 570 C6 dT, /Q670-dT/: Quasar 670 C6 dT, /iCy3/: internal Cy3 modification, /iCy5/: internal Cy5 modification. Oligonucleotides were purchased from Integrated DNA Technologies, ATDBio, or Alpha DNA. 15R60/T8 and 20R25/T4 were designed based on hairpin sequences reported in Ref. (6) and Ref. (7). GC-1 and GC-2 were designed based on sequences used in Ref. (8).

**Table S1. PCR templates, primers, and restriction enzymes used for tether construction.**

	Primers	Length	Template	Digest
TS7700	ttgcgaagaccagattCTTCCTTTCGGCTGAGGTTAATCAC TACTGTTGATGGGTGTCTGGTC	7763	pLC-M6-898-IQ12	BbsI
HP600	gatcgaagacacaatcGCCGTGGATGTGCGACGTATTC ctaagaagactactaaAACGACGGCCAGTGCCAAG	638	pMS-SGS1	BbsI
F500	gatcgaagacacttagACAACCCACAAGTATAGAGGCTCCTATG GACGCGGATATAATGACATTTCTAAC	520	pFO-SE1	BbsI
TE	gaagggctctcagattTACTACTAAGGGCGAATTGGAGCTCC gaagggctctcactaaCACTAAAGGGAACAAAAGCTGGGTAC	4156	pFO-SE2	BsaI
L2F	gatcgaagacacaatcAAGTATGCGCCGCTACAGGGC gatcgaagacagtacATACCGCTCGCCGCAGC	691	pBSII_SK	BbsI

**Table S2. DNA oligonucleotides used for tether construction.**

	Sequence
3-HNDL	/5Phos/TTAGGTGCACG/Q570-dT/AGCT
5-HNDL	TC/Q670-dT/CCATTTTCCTATTACCGGTGCCACGC>
15R60/T8	GCGTGGCACCGGTAATAGGAAAATGGAGA/idSp/GAGTCCTGGATCCTGTTTTTTTTTCAGGAT CCAGGACTC/idSp/AGCTACGTGCAC
20R25/T4	GCGTGGCACCGGTAATAGGAAAATGGAGA/idSp/AAGTTAACATCTAGATTCTATTTTTAGAAAT CTAGATGTTAACTT/idSp/AGCTACGTGCAC
GC-1	/5Phos/ACTGCTGGTACGCGCGCGCGCGCGCG/iCy5/CGCGATCGAC
GC-2	/5Phos/GTCAGTCGATCGCGCGCGCGCGCGCG/iCy3/CGCGTACCAG
MDIG	<GGAAGGAGATTCTCGACAGTTCTAATTGACCTTTACCTTTCCAGTTCAATCTTTGTCAAA CACC
MDIG-C	/5Phos/GGCCATGGTGTGTTGACAAAGATTGAACTGGGAAAAGGTAAGAGGTCAATTAGAACTG TCGAGAATCTCCTTCC
F3	/5Phos/ATGGCCGGGATGCATGGGTTCAACTGC
F4	/5Phos/CAGTGCAGTTGAACCCATGCATCCC

**Note 2. List of parts.** Essential components for adding fluorescence excitation and emission detection paths to the evanescent scattering rotor bead tracking instrument described in Ref. (1). Optical filters were selected for the specific combination of dyes and light sources used in the experiments outlined in the main text. Optics mounting hardware was purchased from Thorlabs, Inc.

- CMOS camera (Mikrotron EoSens CL)
- EMCCD camera (Andor iXon+ 897)
- 532 nm laser (Spectra-Physics Excelsior single-mode, 100 mW)
- 633 nm laser (Melles Griot 25-LHP-925-249, 20 mW)
- Microscope objective (Nikon 60x Apo TIRF, NA 1.49)
- Fiber launch system (Olympus PlanN 10x objective, Thorlabs P1-630PM-FC-2 optical fiber, Thorlabs MBT613D mechanical stage)
- Shutters (nmLaser LST200SLP) with home-built controllers
- Collimator, C1 (Thorlabs F280FC-A)
- Polarizing beam splitter, PBS (Thorlabs PBS121)
- Zero-order quarter wave plate, QWP (Thorlabs WPQ05M-532)
- Lenses, L1 and L2 (Thorlabs A397TM-A and AC254-050-A-ML)
- Lens, L3 (Thorlabs AC254-500-A-ML)
- Mirrors, M1-3 (Thorlabs BB1-E02)
- Coupling mirrors, CM1-2 (Edmund Optics 54-092)
- Iris, I1 (Thorlabs SM1D12C)
- 532 nm notch filter, F1 (Chroma NF03-532E-25)
- 633 nm notch filter, F2 (Chroma NF02-633S-25)
- 755 nm dichroic beamsplitter, DBS2 (Semrock FF775-Di01-25x36)
- 550 nm long-pass filter, F3 (Chroma HHQ550LP)
- 842 nm short-pass filter, F4 (Semrock FF01-842/SP-25)
- 200 mm tube lens, IL1 (Thorlabs ITL200)
- 650 nm dichroic beamsplitter, DBS3 (Semrock FF650-Di01-25x36)
- Lens, L4 ( $\varnothing 25$  mm,  $f \sim 2000$  mm)
- Beam splitter, BS1 (Thorlabs BST11R)
- Lens, L5 ( $\varnothing 25$  mm,  $f = 1000$  mm)
- 2.5x magnifying relay lenses (Nikon)
- Optical splitters, OS1 and OS2 (Cairn Research, OptoSplit II and OptoSplit III)

Mirror M4 and imaging lens IL2 are part of the Nikon Eclipse Ti-S microscope body on which the instrument is built. Unlike Ref. (1), in this work we used a blue fiber-coupled LED (Thorlabs M470F1) for observation of magnetic beads.

## References

1. Lebel, P., A. Basu, F. C. Oberstrass, E. M. Tretter, and Z. Bryant. 2014. Gold rotor bead tracking for high-speed measurements of DNA twist, torque and extension. *Nat. Methods* 11:456-462.
2. Nishizaka, T., Y. Hasimoto, and T. Masaie. 2011. Simultaneous Observation of Chemomechanical Coupling of a Molecular Motor. In *Single Molecule Enzymology: Methods and Protocols*. G. I. Mashanov and C. Batters, editors. Humana Press. Totowa, NJ. 259-271.
3. Kalinin, S., T. Peulen, S. Sindbert, P. J. Rothwell, S. Berger, T. Restle, R. S. Goody, H. Gohlke, and C. A. M. Seidel. 2012. A toolkit and benchmark study for FRET-restrained high-precision structural modeling. *Nat. Methods* 9:1218-1225.
4. Oberstrass, F. C., L. E. Fernandes, and Z. Bryant. 2012. Torque measurements reveal sequence-specific cooperative transitions in supercoiled DNA. *Proc. Natl. Acad. Sci. U.S.A.* 109:6106-6111.
5. Oberstrass, F. C., L. E. Fernandes, P. Lebel, and Z. Bryant. 2013. Torque spectroscopy of DNA: base-pair stability, boundary effects, backbending, and breathing dynamics. *Phys. Rev. Lett.* 110:178103.
6. Woodside, M. T., W. M. Behnke-Parks, K. Larizadeh, K. Travers, D. Herschlag, and S. M. Block. 2006. Nanomechanical measurements of the sequence-dependent folding landscapes of single nucleic acid hairpins. *Proc. Natl. Acad. Sci. U.S.A.* 103:6190-6195.
7. Long, X., J. W. Parks, C. R. Bagshaw, and M. D. Stone. 2013. Mechanical unfolding of human telomere G-quadruplex DNA probed by integrated fluorescence and magnetic tweezers spectroscopy. *Nucleic Acids Res.* 41:2746-2755.
8. Lee, M., S. H. Kim, and S. C. Hong. 2010. Minute negative superhelicity is sufficient to induce the B-Z transition in the presence of low tension. *Proc. Natl. Acad. Sci. U.S.A.* 107:4985-4990.
9. Sarkar, A., R. B. Robertson, and J. M. Fernandez. 2004. Simultaneous atomic force microscope and fluorescence measurements of protein unfolding using a calibrated evanescent wave. *Proc. Natl. Acad. Sci. U.S.A.* 101:12882-12886.
10. Watanabe, T. M., T. Sato, K. Gonda, and H. Higuchi. 2007. Three-dimensional nanometry of vesicle transport in living cells using dual-focus imaging optics. *Biochem. Biophys. Res. Commun.* 359:1-7.
11. Milescu, L. S., C. Nicolai, and J. Bannen. 2000-2013. QuB Software.
12. Roy, R., S. Hohng, and T. Ha. 2008. A practical guide to single-molecule FRET. *Nat. Methods* 5:507-516.
13. Huguet, J. M., C. V. Bizarro, N. Forns, S. B. Smith, C. Bustamante, and F. Ritort. 2010. Single-molecule derivation of salt dependent base-pair free energies in DNA. *Proc. Natl. Acad. Sci. U.S.A.* 107:15431-15436.

14. Zheng, G., X.-J. Lu, and W. K. Olson. 2009. Web 3DNA—a web server for the analysis, reconstruction, and visualization of three-dimensional nucleic-acid structures. *Nucleic Acids Res.* 37:W240-W246.
15. Stein, I. H., V. Schüller, P. Böhm, P. Tinnefeld, and T. Liedl. 2011. Single-Molecule FRET Ruler Based on Rigid DNA Origami Blocks. *ChemPhysChem* 12:689-695.
16. Woźniak, A. K., G. F. Schröder, H. Grubmüller, C. A. M. Seidel, and F. Oesterhelt. 2008. Single-molecule FRET measures bends and kinks in DNA. *Proc. Natl. Acad. Sci. U.S.A.* 105:18337-18342.
17. Choi, U. B., P. Strop, M. Vrljic, S. Chu, A. T. Brunger, and K. R. Weninger. 2010. Single-molecule FRET-derived model of the synaptotagmin 1-SNARE fusion complex. *Nat. Struct. Mol. Biol.* 17:318-324.